

A MULTI-WAVELENGTH STUDY OF NEARBY MILLISECOND PULSAR PSR J1400–1431: IMPROVED ASTROMETRY & AN OPTICAL DETECTION OF ITS COOL WHITE DWARF COMPANION

J. K. SWIGGUM¹, D. L. KAPLAN¹, M. A. MCLAUGHLIN^{2,3}, D. R. LORIMER^{2,3}, S. BOGDANOV⁴, P. S. RAY⁵, R. LYNCH^{6,3},
P. GENTILE^{2,3}, R. ROSEN⁷, S. A. HEATHERLY⁶, B. N. BARLOW⁸, R. J. HEGEDUS⁸, A. VASQUEZ SOTO⁸, P. CLANCY⁸, V. I.
KONDRATIEV^{9,10}, K. STOVALL^{11,12}, A. ISTRATE¹, B. PENPRASE¹³, E. C. BELLM¹⁴

Draft version September 1, 2017

ABSTRACT

In 2012, five high school students involved in the Pulsar Search Collaboratory discovered the millisecond pulsar PSR J1400–1431 and initial timing parameters were published in Rosen et al. (2013) a year later. Since then, we have obtained a phase-connected timing solution spanning five years, resolving a significant position discrepancy and measuring \dot{P} , proper motion, parallax, and a monotonic slope in dispersion measure over time. Due to PSR J1400–1431’s proximity and significant proper motion, we use the Shklovskii effect and other priors to determine a 95% confidence interval for PSR J1400–1431’s distance, $d = 270_{-80}^{+130}$ pc. With an improved timing position, we present the first detection of the pulsar’s low-mass white dwarf (WD) companion using the Goodman Spectrograph on the 4.1-m SOAR telescope. Deeper imaging suggests that it is a cool DA-type WD with $T_{\text{eff}} = 3000 \pm 100$ K and $R/R_{\odot} = (2.19 \pm 0.03) \times 10^{-2}$ ($d/270$ pc). We show a convincing association between PSR J1400–1431 and a γ -ray point source, 3FGL J1400.5–1437, but only weak ($3.3\text{-}\sigma$) evidence of pulsations after folding γ -ray photons using our radio timing model. We detect an X-ray counterpart with *XMM-Newton* but the measured X-ray luminosity (1×10^{29} ergs s⁻¹) makes PSR J1400–1431 the least X-ray luminous rotation-powered millisecond pulsar (MSP) detected to date. Together, our findings present a consistent picture of a nearby ($d \approx 230$ pc) MSP in a 9.5 day orbit around a cool, $\sim 0.3 M_{\odot}$ WD companion, with orbital inclination, $i \gtrsim 60^{\circ}$.

1. INTRODUCTION

PSR J1400–1431 is a 3.08 ms radio pulsar discovered by Pulsar Search Collaboratory (PSC) students (Rosen et al. 2013) in a portion of the Green Bank 350 MHz Drift Scan Survey (Boyles et al. 2013; Lynch et al. 2013). With a dispersion measure (DM) of 4.9 pc cm^{-3} , it is one of only five millisecond pulsars (MSPs) with $\text{DM} < 5 \text{ pc cm}^{-3}$. Since DM provides a measure of the electron content along the line of sight, it can be used as a proxy for distance, given Galactic electron density models (e.g. Taylor & Cordes 1993; Cordes & Lazio 2002; Yao et al.

2017). Yao et al. (2017) describe the most recent electron density model, which predicts that J1400–1431 has a distance of only 350 pc.

Nearby MSPs allow high-precision measurements of astrometric parameters like proper motion and, in some cases, parallax through pulsar timing. The latter involves detecting the curvature of incoming wavefronts – a signature only found in timing residuals for a handful of nearby MSPs close to the ecliptic plane (Kaspi et al. 1994; Camilo et al. 1994a; Sandhu et al. 1997; Wolszczan et al. 2000; Jacoby et al. 2003; Hotan et al. 2004a; Löhmer et al. 2004; Splaver et al. 2005; Reardon et al. 2016; Desvignes et al. 2016; Matthews et al. 2016). However, parallax has also been detected using very long baseline interferometry (VLBI) follow-up in many other cases (Briskin et al. 2002; Chatterjee et al. 2009). Together, distance and DM provide an average measure of free electrons along the line of sight to the pulsar (Toscano et al. 1999a; Lommen et al. 2006); combined with proper motion, transverse velocities can be derived to study an underlying distribution for MSPs (Toscano et al. 1999b) and compare it to velocity distributions for other sub-populations. Underlying velocity distributions provide estimates for pulsars’ natal kicks from the supernova explosions that created them (Hobbs et al. 2005).

Because of its proximity and brightness, J1400–1431 was considered for inclusion in pulsar timing arrays (PTAs; e.g. Demorest et al. 2013; Arzoumanian et al. 2015), but was dropped due to inconsistent detectability at 820 MHz and higher observing frequencies. Rosen et al. (2013) hypothesized that unreliable detections at higher frequencies were likely due to J1400–1431’s particularly steep spectrum.

We used a novel drift-scan technique to improve localization for this pulsar (see further discussion in Gentile & Swiggum, in prep.), finding a position that differed by $6.7'$ from that published in Rosen et al. (2013). This dif-

¹ Center for Gravitation, Cosmology and Astrophysics, Department of Physics, University of Wisconsin–Milwaukee, P.O. Box 413, Milwaukee, WI 53201, USA

² Department of Physics and Center for Gravitational Waves and Cosmology, West Virginia University, White Hall, Morgantown, WV 26506, USA

³ Center for Gravitational Waves and Cosmology, West Virginia University, Chestnut Ridge Research Building, Morgantown, WV 26505

⁴ Columbia Astrophysics Laboratory, Columbia University, New York, NY 10027, USA

⁵ Space Science Division, Naval Research Laboratory, Washington, DC 20375-5352, USA

⁶ Green Bank Observatory, PO Box 2, Green Bank, WV, 24944, USA

⁷ NRAO, 520 Edgemont Road, Charlottesville, VA 22903, USA

⁸ One University Parkway, Department of Physics, High Point University, High Point, NC 27268

⁹ ASTRON, The Netherlands Institute for Radio Astronomy, Postbus 2, 7990 AA, Dwingeloo, The Netherlands

¹⁰ Astro Space Centre, Lebedev Physical Institute, Russian Academy of Sciences, Profsoyuznaya Str. 84/32, Moscow 117997, Russia

¹¹ NRAO, PO Box 0, Socorro, NM 87801, USA

¹² Dept. of Physics and Astronomy, Univ. of New Mexico, NM 87131, USA

¹³ Department of Physics & Astronomy, Pomona College, 610 N. College Ave., Claremont, CA 91711, USA

¹⁴ Department of Astronomy, University of Washington, Seattle, WA 98195

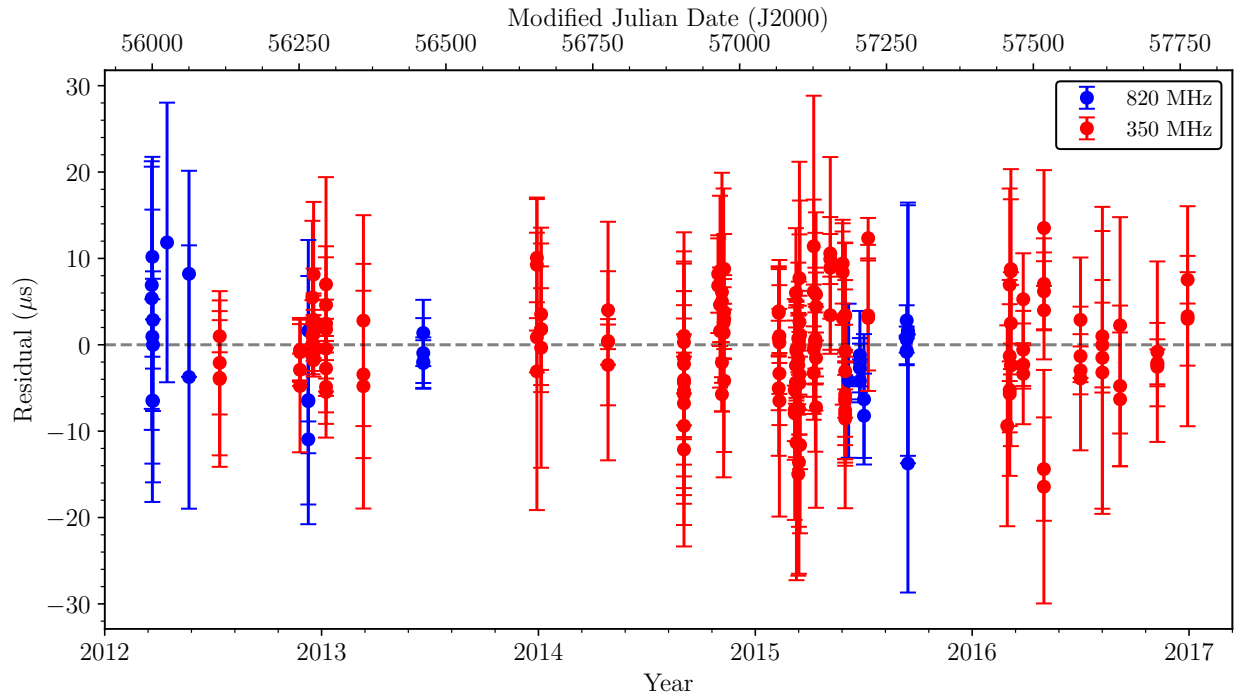


Figure 1. Timing residuals in microseconds for J1400–1431, showing observations at 350 MHz (red) and 820 MHz (blue), respectively.

ference is larger than the formal uncertainty, but since the previous timing solution was based on less than one year of timing data, it is subject to significant covariance between position and spin-down parameters. The offset also undoubtedly played a significant role in early detectability issues at higher frequencies. In this paper, we present an improved, phase-connected timing solution for J1400–1431 with pulse times of arrival (TOAs) spanning five years, including those published in Rosen et al. (2013). The significantly longer timing baseline compared to that of the previous study rules out any covariance between fits for position and spin-down.

In §2, we provide a detailed description of our full radio timing analysis, including measurements of proper motion, a linear slope in DM over time, and first and second Laplace parameters (effectively the orbital eccentricity). We have also developed a posterior probability distribution for J1400–1431’s distance based on a timing parallax fit, combined with several other priors.

Nearby MSPs are also good candidates for multi-wavelength follow-up. In §3, we describe our observing campaign and photometry analysis using the Keck Low-Resolution Imaging Spectrometer (LRIS) and the Southern Astrophysical Research (SOAR) optical telescopes to image J1400–1431’s white dwarf (WD) companion. PSR J1400–1431 has spin and orbital parameters similar to other low-mass binary pulsars (LMBPs) – namely, its short spin period ($P < 10$ ms), small eccentricity ($e < 10^{-3}$), and a minimum companion mass, $m_{c,\min} = 0.26 M_{\odot}$, which falls in a typical range for LMBPs, $0.15 M_{\odot} < m_c < 0.4 M_{\odot}$. These systems are thought to evolve from a neutron star accreting material from a low-mass star in its giant phase. Stable mass transfer causes the neutron star to spin faster, while its companion (provided $m_c \lesssim 1.6 M_{\odot}$) does not undergo helium ignition in its core, resulting in a binary system containing a MSP and a low-mass He-core WD (Phinney & Kulkarni 1994).

In §4 and §5 respectively, we describe γ -ray and X-ray detections, which also help constrain the pulsar’s dis-

tance and spin period derivative (\dot{P}), taking into account respective emission efficiencies (e.g. Guillemot et al. 2016; Becker 2009; Prinz & Becker 2015). We synthesize and discuss the collected information from multi-wavelength follow-up in §6 and summarize our conclusions in §7.

2. RADIO OBSERVATIONS & TIMING ANALYSIS

In order to improve upon the preliminary timing solution published in Rosen et al. (2013), we include those data here, but have reprocessed them according to the procedure described below. All timing observations were conducted with the Robert C. Byrd Green Bank Telescope (GBT) at either 350 or 820 MHz using the Green Bank Ultimate Pulsar Processing Instrument (GUPPI; DuPlain et al. 2008) with 100 or 200 MHz bandwidth, respectively, and sampled every $81.92 \mu\text{s}$. Since J1400–1431 has not been observed as part of a dedicated timing proposal since 2013, many of the more recent TOAs come from using the pulsar to conduct test scans before Green Bank North Celestial Cap (GBNCC; Stovall et al. 2014) survey observations. Because of this, the set-up/observing parameters changed slightly for different groups of TOAs, so we noted these changes and carefully accounted for any resulting systematics (e.g. GUPPI offsets; see Table 1). Also, because of its frequent use as a test source, many scans were taken using incoherent search-mode (rather than coherent fold-mode), resulting in relatively coarse time sampling for MSP monitoring.

We identified the highest signal-to-noise ratio detections at each observing frequency after folding data with the correct spin period and DM at each epoch, then fit three Gaussians to the corresponding pulse profiles to generate noiseless standard profiles. Standard profiles were aligned using `pas` from PSRCHIVE¹⁵ (Hotan et al. 2004b).

We zapped RFI interactively with `pazi` and used standard profiles to generate four TOAs per epoch with `pat`

¹⁵ <http://psrchive.sourceforge.net/>

Table 1
Details of Observing Modes Used for PSR J1400–1431

Center Frequency (MHz)	Bandwidth (MHz)	N_{channels}	t_{sample} (μs)	Observing Mode	GUPPI Offset ^a (μs)	N_{TOA}
350	100	2048	81.92	Incoherent	40.96	52
350	100	4096	81.92	Incoherent	81.92	101
350	100	128	1.28	Coherent Fold	7.68	17
820	200	2048	81.92	Incoherent	20.48	16
820	200	128	0.64	Coherent Fold	3.84	17

^a Mode-dependent instrumental timing offsets used for PSR J1400–1431.

Table 2
Measured and derived timing parameters for PSR J1400–1431

Parameter	Value
Spin & Astrometric Parameters	
Ecliptic Longitude (J2000).....	213.11368082(8)
Ecliptic Latitude (J2000).....	-2.1064331(18)
Proper Motion in Ecliptic Lon. (mas/yr)	34.75(19)
Proper Motion in Ecliptic Lat. (mas/yr)	-46(6)
Parallax (mas).....	3.6(11)
Spin Period (s).....	0.00308423326039194(8)
Period Derivative (s/s).....	$7.2333(15) \times 10^{-21}$
Intrinsic Period Derivative (s/s).....	$< 2.2 \times 10^{-21}$
Dispersion Measure (pc cm ⁻³).....	4.93258(3)
$d\text{DM}/dt$ (pc cm ⁻³ yr ⁻¹).....	$1.8(3) \times 10^{-4}$
Reference Epoch (MJD).....	56960.0
Span of Timing Data (MJD).....	56006-57751
Number of TOAs.....	203
RMS Residual (μs).....	4.06
EFAC.....	1.8
Binary Parameters ^a	
Orbital Period (days).....	9.5474676743(19)
Projected Semi-major Axis (lt-s).....	8.4212530(6)
Epoch of Ascending Node (MJD).....	56958.38397673(9)
First Laplace Parameter.....	$2.8(12) \times 10^{-7}$
Second Laplace Parameter.....	$4.8(14) \times 10^{-7}$
Derived Parameters	
Right Ascension (J2000).....	14:00:37.00370(15)
Declination (J2000).....	-14:31:47.0422(6)
Orbital Eccentricity.....	$5.5(14) \times 10^{-7}$
Surface Magnetic Field (10 ⁷ Gauss).....	< 8.3
Spin-down Luminosity (10 ³³ erg/s).....	< 3.0
Characteristic Age (Gyr).....	> 22
Total Proper Motion (mas/yr).....	57(5)
Transverse Velocity ^b (km/s).....	76(20)
Shklovskii Period Derivative ^b (s/s).....	$7(2) \times 10^{-21}$
Mass Function (M_{\odot}).....	0.0070345527(14)
Minimum Companion Mass ^c (M_{\odot}).....	0.26

Note. — Quantities are listed with 68% ($1\text{-}\sigma$) uncertainties on the last digit in parentheses. The intrinsic spin-down (\dot{P}_{int}) is constrained by $\dot{P}_{\text{Shklov}} = 5 \times 10^{-21}$; upper/lower limits on other derived parameters come from \dot{P}_{int} , assuming the pulsar’s moment of inertia $I = 10^{45}$ g cm² and a 90° offset between its rotational and magnetic axes.

^a Using the ELL1 binary timing model.

^b Computed using the distance derived from the timing parallax measurement with no correction.

^c Calculated assuming a pulsar mass, $m_p = 1.35 M_{\odot}$.

– summing across time and averaging down to four frequency subbands. Most of our observations were taken at 350 MHz, so retaining some frequency-dependence in our TOAs allowed us to fit for a linear slope in DM over our entire data span ($d\text{DM}/dt$). In order to phase-connect the entire dataset, we fit for spin, position, proper motion, DM, and binary parameters (see Table 2). Param-

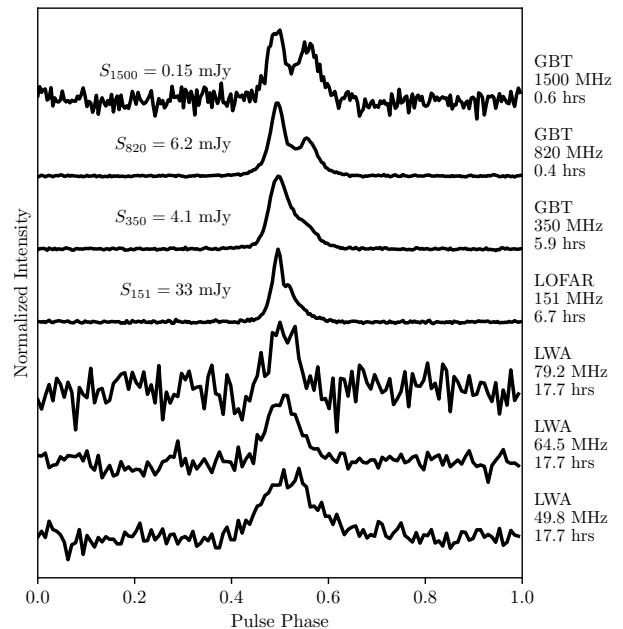


Figure 2. Integrated profiles for J1400–1431 show radio intensity as a function of pulse phase at a variety of observing frequencies spanning 50–1500 MHz. Profiles obtained with LWA and LOFAR/GBT observations are plotted here with 128 and 256 bins, respectively. Frequency-dependent flux values (e.g. S_{1500}) are shown next to corresponding profiles, each with $\sim 50\%$ uncertainty.

eter fits were carried out with TEMPO¹⁶ timing software and the DE421 Solar System ephemeris; the timing solution is referenced to UTC (NIST). Due to J1400–1431’s small eccentricity, we used the ELL1 binary model, described originally in Appendix A of Lange et al. (2001). The parameter uncertainties shown in Table 2 reflect $1\text{-}\sigma$ (68%) uncertainties on measured parameters. However, a global, multiplicative error factor (EFAC) has been applied to individual TOA errors such that the resulting reduced χ^2 value is one. Fitting for all parameters in our current timing solution results in 4 μs root-mean-square (RMS) residuals with no obvious systematic trends (see Figure 1).

The position reported in Table 2 differs from that published in Rosen et al. (2013) by 6.7’; that timing solution was based on data spanning less than a year and therefore, was likely affected by position/spin-down covariance. We found an initial phase-coherent timing solution for J1400–1431 spanning several years in late June of 2015 and started observing it using the corrected position shortly afterwards (MJD 57199). For 350/820 MHz GBT observations, a 6.7’ position offset results in a 9/43% degradation in gain respectively. Since the majority of our timing observations were conducted at 350 MHz, the

¹⁶ <http://tempo.sourceforge.net/>

offset did not result in a significant loss of sensitivity.

2.1. Flux Density Estimates & Scintillation

We re-folded existing data and aligned profiles using our new timing solution, then summed profiles from separate frequency bands in-phase using `psradd` (see Figure 2). Figure 2 also includes relatively short test scans taken with the GBT at 820 MHz and 1500 MHz at the best-fit timing position. With GBT data, we estimated flux densities between 350–1500 MHz by measuring signal-to-noise ratios in each case and applying the radiometer equation (see e.g., Lorimer & Kramer 2004). PSR J1400–1431 was first detected at low frequency in a LOw-Frequency ARray (LOFAR; van Haarlem et al. 2013) census of MSPs (Kondratiev et al. 2016), but we obtained additional data for further study to generate the profile shown in Figure 2. With LOFAR data, we measured calibrated flux densities from 15 observations conducted over a ~ 6 month period and quote the median value with 50% uncertainties ($S_{151} = 33 \pm 16$ mJy) since we did not carefully account for flux density variations due to J1400–1431 getting close to the Sun during this observing campaign and difficulties in calibrating LOFAR pulsar flux density measurements (Murphy et al. 2017). We assume similar uncertainties for GBT flux density estimates, although they are likely even higher for nominal S_{820} and S_{1500} values since we do not yet have enough detections in these bands to average over flux density variability due to scintillation and other effects. Although scintillation may still be problematic for consistent detectability given its low DM, test observations at 820 MHz and 1500 MHz suggest that J1400–1431 should be re-evaluated for PTA inclusion.

Finally, Figure 2 shows summed profiles for J1400–1431 in three frequency bands (49.8 MHz, 64.5 MHz, and 79.2 MHz – each with 19.6 MHz bandwidth) obtained with the Long Wavelength Array (LWA; e.g. Taylor et al. 2012). As of 2015, only three other MSPs were detected in an initial census (Stovall et al. 2015), so J1400–1431 is one of very few MSPs detected at these low frequencies. Since we have not yet carefully accounted for flux density variations due to a variety of known factors (e.g. frequency, zenith angle, and local sidereal time), we omit flux density estimates for the LWA detections shown in Figure 2.

Due to J1400–1431’s low DM, we expect it so scintillate heavily, and we see evidence of this in the significantly tailed distribution of 350 MHz TOA weights. However, looking at dynamic spectra from individual observations, there are no visible scintles, indicating that the scintillation timescale and bandwidth are too large to be resolvable by these observations. Because the scintillation timescales and bandwidths are not measurable in our data, we rely on estimates from the NE2001 (Cordes & Lazio 2002) electron density model to better understand J1400–1431’s scintillation behavior. For the GBT profiles shown in Figure 2, only the one at 350 MHz incorporates enough data to average out the effect of scintillation. That is, the total integration time (5.9 hours) far exceeds the scintillation timescale at 350 MHz ($\Delta t_{\text{DISS},350} \approx 25$ mins). In all cases, scintillation bandwidths are comparable to our observing bandwidths, but at higher frequencies, the scintillation timescales ($\Delta t_{\text{DISS},820} \approx 35$ mins and $\Delta t_{\text{DISS},1500} \approx 45$ mins) exceed the total integration time for each profile. This suggests that corresponding estimated flux densities in these cases do not properly account for the effects

of scintillation and are therefore somewhat biased.

2.2. Constraining Distance

Given J1400–1431’s position and dispersion measure ($\text{DM} = 4.9 \text{ pc cm}^{-3}$), Galactic electron density models provide distance estimates along the pulsar’s line of sight: 270 pc (Taylor & Cordes 1993), 500 pc (Cordes & Lazio 2002), and most recently, 350 pc (Yao et al. 2017). Normally, DM distances can be highly uncertain, particularly for pulsars with high Galactic latitudes like J1400–1431 ($b = 45^\circ$). In comparison with earlier Galactic electron density models, Yao et al. (2017) improve on distance estimates for pulsars with $|b| > 40^\circ$ whose distances have been measured independently. For 80% of these pulsars, Yao et al. (2017) predict DM distances with uncertainties $< 40\%$, but for some nearby MSPs we can measure distances to higher precision with pulsar timing. In some cases, the curvature of incoming wavefronts (Backer & Hellings 1986) can be measured as a 6-month periodic signature in timing residuals with amplitude,

$$A_\varpi = \frac{l^2 \cos^2 \beta}{2cd}, \quad (1)$$

where A_ϖ is the amplitude of the timing parallax signature, β and d are the pulsar’s ecliptic latitude and distance respectively, l is the Earth-Sun distance (1 AU) and c is the speed of light. Because of nearby distance estimates and its low ecliptic latitude ($\beta = 2.1^\circ$), we decided to include parallax in J1400–1431’s pulsar timing model (see Table 2) and detected it ($\varpi = 3.6 \pm 1.1$ mas) with $\sim 3\text{-}\sigma$ significance. This measurement constrains the system’s distance inside the range $170 < d/\text{pc} < 710$ with 95% confidence, but the distribution is weighted towards larger distances since $d \propto 1/\varpi$ (see cyan curve in Figure 3). We further refined these distance constraints using additional astrometric information.

Originally shown by Shklovskii (1970), the induced period derivative due to secular acceleration (\dot{P}_{Shklov}) can account for a significant fraction of the measured spin-down (\dot{P}_{meas}), which is composed of both intrinsic and kinematic components, $\dot{P}_{\text{meas}} = \dot{P}_{\text{int}} + \dot{P}_{\text{Shklov}}$. Following Nice & Taylor (1995), we also investigated the contributions on \dot{P}_{meas} due to the pulsar’s acceleration perpendicular to the Galactic plane (2.4×10^{-22} s/s, or 3% of \dot{P}_{meas}) and due to differential Galactic rotation (1.4×10^{-23} s/s, or 0.2% of \dot{P}_{meas}). These effects are more than an order of magnitude smaller than \dot{P}_{Shklov} , so we consider them negligible for the discussion that follows. Assuming J1400–1431 is spinning down ($\dot{P}_{\text{int}} > 0$) and by imposing the constraint $\dot{P}_{\text{meas}} > \dot{P}_{\text{Shklov}}$, we place an upper limit on the pulsar’s distance and therefore, a lower limit on its parallax.

We constrain the distance jointly through the parallax measurement and the Shklovskii effect, also applying corrections for the Lutz-Kelker bias (Lutz & Kelker 1973). Adopting the notation of Verbiest et al. (2010), we attempt to determine the true parallax ϖ given the measurement ϖ_0 via,

$$p(\varpi|\varpi_0) = \frac{p(\varpi_0|\varpi)p(\varpi)}{p(\varpi_0)}, \quad (2)$$

where we use a normal distribution for $p(\varpi_0|\varpi) = \mathcal{N}(\varpi_0, \sigma_\varpi) = \exp(-(\varpi_0 - \varpi)^2/2\sigma_\varpi^2)/\sqrt{2\pi\sigma_\varpi^2}$ and take $p(\varpi_0)$ to be flat. We use a volumetric prior for ϖ to

account for the Lutz-Kelker bias,

$$p_D(\varpi) \propto \varpi^{-4}, \quad (3)$$

and add an additional term to the prior to account for the Shklovskii effect. We infer a distribution on the distance based on the proper motion μ and spin-down,

$$\varpi_{\text{Shklov}} = \left(\frac{-\dot{f}}{c(\dot{f}_{\text{meas}} - \dot{f}_{\text{int}})} \right) \mu^2 = A\mu^2, \quad (4)$$

with $A = -\dot{f}/c(\dot{f}_{\text{meas}} - \dot{f}_{\text{int}})$. We take the proper motion to be given by $p(\mu_0|\mu) = \mathcal{N}(\mu_0, \sigma_\mu)$. Note that we have implicitly assumed that the parallax and proper motion distributions are independent (i.e. not correlated), but have verified this through exploration of the parameter space and believe it to be a robust assumption. Then, with the constraint that $\dot{f}_{\text{int}} \leq 0$, we get a lower limit on ϖ given by the cumulative integral of the distribution of $p(\mu_0|\mu)$ transformed to ϖ ,

$$p_\mu(\varpi) = \int_0^\varpi d\varpi' \frac{1}{\sqrt{8\pi A \varpi' \sigma_\mu^2}} e^{-(\sqrt{\varpi'/A} - \mu_0)^2 / 2\sigma_\mu^2} \quad (5)$$

suitably normalized. Our final prior distribution $p(\varpi)$ is the product of $p_D(\varpi)$ and $p_\mu(\varpi)$, resulting in 95% confidence intervals on parallax and distance of $\varpi = 3.7^{+1.6}_{-1.2}$ mas and $d = 270^{+130}_{-80}$ pc, respectively. We use the confidence interval on distance to show corresponding parallax signatures in Figure 4, computed using Equation 1. In this figure, we also show binned timing residuals to illustrate the parallax signature measured with pulsar timing techniques described earlier.

We checked the parallax fit with a bootstrap method (Efron 1979), generating 50,000 sets of TOAs by randomly sampling the original TOAs with replacement until each trial set had the same number of TOAs as the original. Starting with our best-fit timing solution, we re-fit for all parameters using each trial TOA file and recorded trial fit parameters.

Overall, the bootstrap reproduced the conclusions from our best-fit timing solution once we excluded non-physical results (such as negative parallax). The widths of the bootstrap posterior distributions for individual parameters were somewhat larger than uncertainties reported by TEMPO, by a factor of 1–2 depending on the parameter. However, our conclusions remain largely unchanged: even if we assume a factor of 2 increase in the parallax uncertainties, the effect on the 95% confidence interval for the distance is negligible, going from 190–400 pc to 160–420 pc. We are obtaining more data as well as investigating further timing techniques to fully reconcile this issue.

3. OPTICAL FOLLOW-UP

We used the Goodman Spectrograph on the 4.1-m SOAR Telescope (Clemens et al. 2004) in its imaging mode to obtain optical photometry of a $6' \times 6'$ field surrounding PSR J1400–1431. The object frames were bias-subtracted and flat-fielded using CCDPROC and other standard routines in IRAF¹⁷ (Tody 1986) and averaged together using the IMCOMBINE routine to create a final,

¹⁷ IRAF is distributed by the National Optical Astronomy Observatories, which are operated by the Association of Universities for Research in Astronomy, Inc., under cooperative agreement with the National Science Foundation.

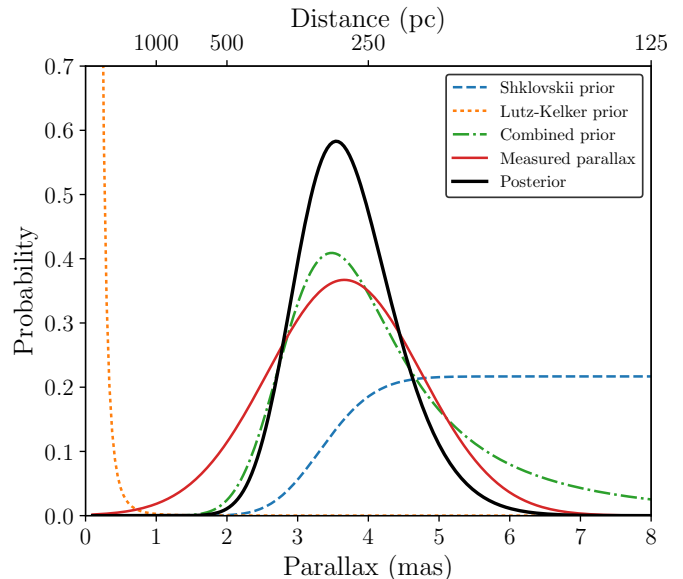


Figure 3. Posterior probability distribution function (black line) for the distance of PSR J1400–1431, based on Eqn. 5 for an intrinsic spin-down $\dot{f} = 0$. We also show the distribution from the measured parallax (red line), the prior derived from the limit on the distance due to the Shklovskii effect (blue dashed line), the volumetric prior for the Lutz-Kelker correction (Eqn. 3; orange dotted line), and the combined prior distribution (green dash-dotted line).

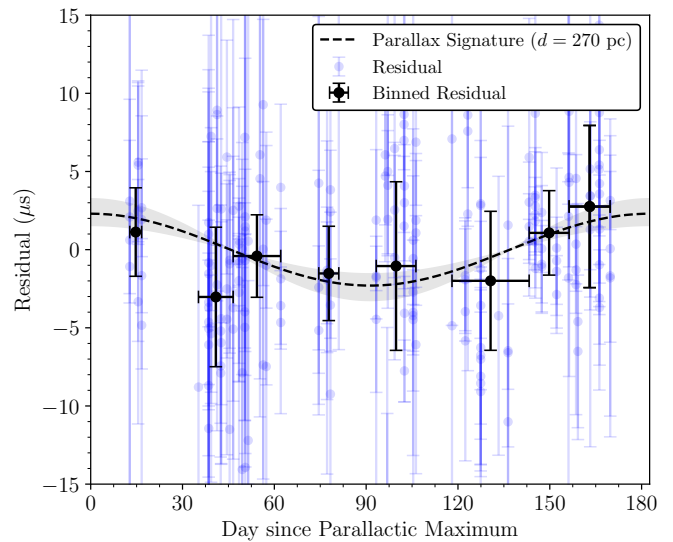


Figure 4. Timing residuals and uncertainties for J1400–1431 (light blue), folded over a 6-month period and binned over stretches of less than 20 days. Day zero is defined as the time at which the Earth-Sun-pulsar angle is 90° (parallaxic maximum). Black points show residuals’ averages, weighted by their uncertainties squared. Due to uneven sampling, groups of residuals spanning ≤ 20 days were chosen to exclude gaps longer than 10 days and horizontal error bars show the extent of residuals that were averaged. The shaded region shows the range of expected parallax signature amplitudes in the residuals for distances that correspond to limits from our 95% confidence interval, $190 < d < 400$ pc ($6.5 > A_\varpi > 3.1 \mu\text{s}$). The dashed line shows $A_\varpi = 4.6 \mu\text{s}$, the expected amplitude of a timing parallax signature corresponding to the system’s highest probability distance, $d = 270$ pc.

master frame. We then ran the master frame through *astrometry.net* (Lang et al. 2010) to obtain an astrometric calibration to a precision of better than $0.1''$.

A visual inspection of the master object frame, a subset of which is shown in Figure 5, reveals a faint optical source at the precise location of J1400–1431 deter-

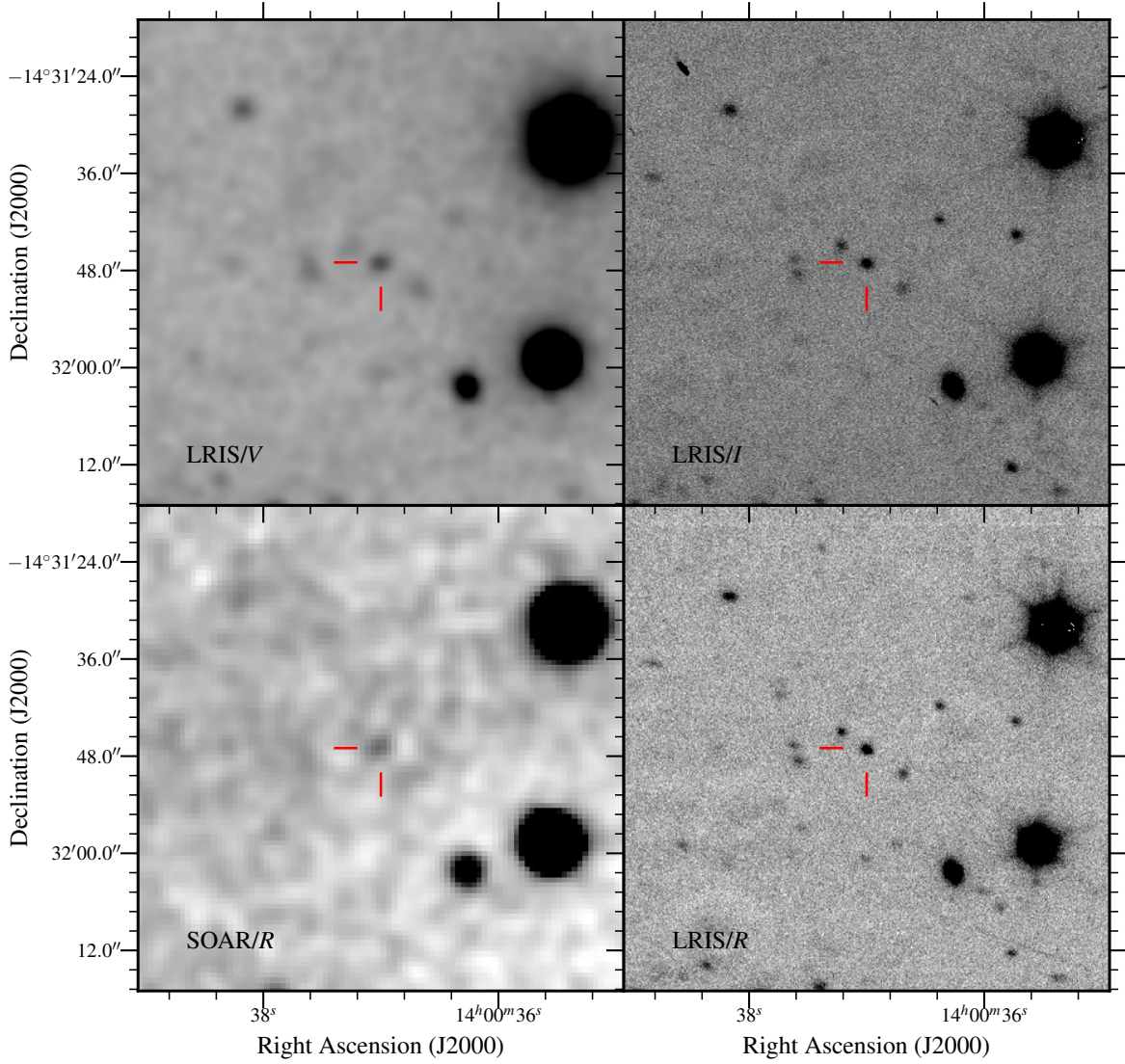


Figure 5. The region around the radio position of PSR J1400–1431, with data from Keck I/LRIS in the V (upper left), R (lower right) and I (upper right) filters. We also show the same region with data from SOAR/Goodman in the R_c filter. Each image is $1'$ on a side, with north up and east to the left. The radio position of PSR J1400–1431 is shown with the tick marks. For the LRIS/ V and SOAR/ R_c images we have additionally smoothed the data to improve the visibility of the counterpart.

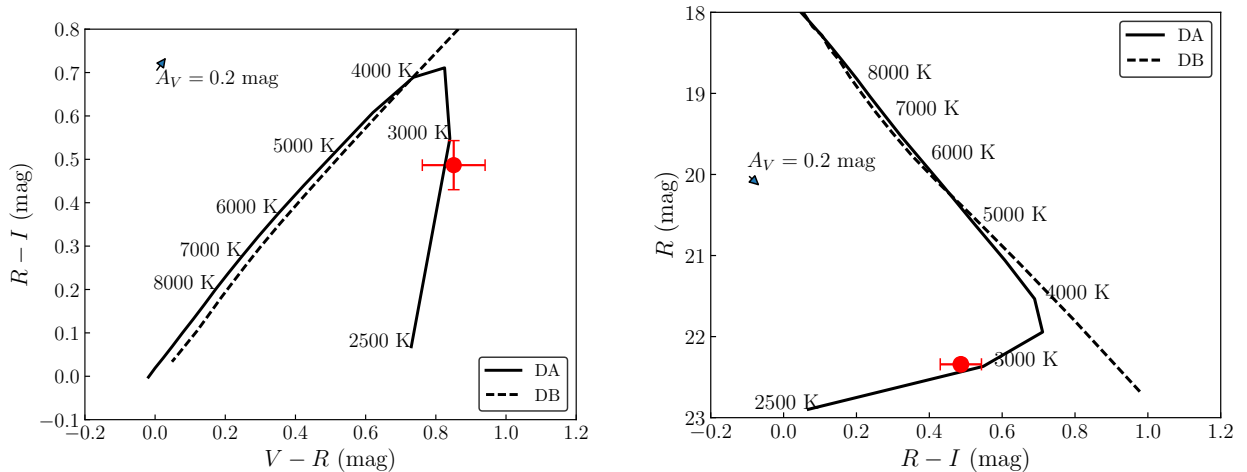


Figure 6. Color-color (left) and color-magnitude (right) diagrams for PSR J1400–1431, based on the photometry in Table 3. The color-color diagram shows the $R - I$ color vs. the $V - R$ color along with synthetic photometry from Tremblay et al. (2011) and Bergeron et al. (2011) for hydrogen (DA; solid line) and helium (DB; dashed line), respectively. The synthetic photometry is labeled with the effective temperature, and the arrow shows a reddening vector for $A_V = 0.2$. The color-magnitude diagram shows the R magnitude vs. the $R - I$ color with the same synthetic photometry models, which have been adjusted to have a radius of $0.0219 R_\odot$ at a distance of 270 pc.

mined from the radio observations. We used the PHOT task in the IRAF/DAOPHOT package to extract aperture photometry of nearly two dozen stars in the field of view of the master frame, covering a range of magnitudes $R_c \simeq 15 - 20$. Our measured magnitude for each star was compared to the values reported by Qi et al. (2015) in order to determine the zero-point magnitude of our data set, after converting their R_F photographic red band magnitudes to R_c via the transformations of Bessell (1986). We then used PHOT to perform aperture photometry on the optical component of J1400–1431 and derived a final R_c -band magnitude of $R_c = 22.5 \pm 0.3$.

We obtained additional, deeper imaging of J1400–1431 using the blue and red sides of the Low-Resolution Imaging Spectrometer (LRIS; Oke et al. 1995) on the 10-m Keck I telescope. The data were reduced using standard procedures in IRAF, subtracting the bias, dividing by flatfields, and combining the individual exposures. At this time J1400–1431 was only visible during the very beginning of the night, so the observations were obtained at somewhat high airmass (up to 2.0).

Guided by the SOAR detection, we were able to detect the counterpart to J1400–1431 in all three bands of the LRIS imaging as seen in Figure 5. We reduced the LRIS data using standard procedures provided by the LPIPE reduction framework.¹⁸ Astrometric calibration was performed against USNO-B (Monet et al. 2003) and RMS scatter against the catalog was $\sim 0.4''$ for 16-19 matched sources. Aperture photometry was measured using SExtractor (Bertin & Arnouts 1996). We photometrically calibrated the LRIS images using the Pan-STARRS 3π Steradian Survey (Chambers et al. 2016; Flewelling et al. 2016) catalog.¹⁹ In each image we identified ~ 20 stars that matched those from the catalog and were additionally not extended, saturated, or otherwise affected by bad pixels. We transformed the Pan-STARRS photometry to the Johnson-Cousins system using the results from Tonry et al. (2012) and determined zero-points for each LRIS image. Comparing observations of 15 other stars detected by both SOAR (in R_c) and Keck (in R), we found consistent results.

In Figure 6 we plot these results on color-color and color-magnitude diagrams along with the predictions of model atmospheres for hydrogen (DA) and helium (DB) white dwarf atmospheres from Tremblay et al. (2011) and Bergeron et al. (2011), respectively.²⁰ From the color-color diagram it appears that the $R-I$ color is consistent either with an effective temperature $T_{\text{eff}} \approx 4800$ K or $T_{\text{eff}} \approx 3000$ K. This degeneracy is a result of collisionally-induced absorption by molecular H_2 (Bergeron, Saumon, & Wesemael 1995; Hansen 1998), which shifts flux from the near-infrared into the optical. However, from the $V-R$ color only the cooler solution seems plausible. Fitting the extinction-corrected photometry as a function of T_{eff} and angular size, we get a good solution for $T_{\text{eff}} = 3000 \pm 100$ K and $R/R_\odot = (2.19 \pm 0.03) \times 10^{-2}$ ($d/270$ pc), where we have increased the uncertainty on T_{eff} to account for the coarseness of our atmosphere grid.

4. GAMMA-RAY SPECTRA AND TIMING

¹⁸ <http://www.astro.caltech.edu/~dperley/programs/lpipe.html>

¹⁹ The counterpart is visible directly in Pan-STARRS (PS1) stacked r and i band images, but is not listed in the corresponding catalog, suggesting a low significance detection. In any case we did not use PS1 to motivate followup because the data were released after discovery of the counterpart with SOAR.

²⁰ [http://www.astro.umontreal.ca/~sim\\$bergeron/CoolingModels/](http://www.astro.umontreal.ca/~sim$bergeron/CoolingModels/)

The radio timing position of PSR J1400–1431 reported in Table 2 is within $5.3'$ of the *Fermi* Large Area Telescope (LAT) source 3FGL J1400.5–1437 (which has a 95% confidence error ellipse of size $7.0' \times 4.7'$). A positional association was noted by Acero et al. (2015) and in the following discussion, we analyze the γ -ray source to evaluate the likelihood of an association and to search for evidence of γ -ray pulsations.

For this analysis, we extracted Pass 8 data starting from 2008 August 4 (the beginning of LAT survey mode operation) and extending through 2017 March 1 (Mission Elapsed Time 239557517 – 510019205). We selected SOURCE class, front and back-converting events (`evclass = 128` and `evtype = 3`) combined during the intervals of good science data (`DATA_QUAL=1` and `LAT_CONFIG=1`) and restricted our events to those with a zenith angle less than 90° . We selected events between 100 MeV and 100 GeV from a 15° radius around the pulsar and performed a binned likelihood analysis over a $20^\circ \times 20^\circ$ region with 0.1° pixels. Starting with a model based on the 3FGL catalog (Acero et al. 2015), we modified the target source’s spectral model to be an exponentially cutoff power law of the form,

$$\frac{dN}{dE} = N_0 \left(\frac{E}{E_0} \right)^{-\Gamma} \exp \left(-\frac{E}{E_{\text{cut}}} \right), \quad (6)$$

with normalization N_0 in photons $\text{cm}^{-2} \text{s}^{-1} \text{MeV}^{-1}$, reference energy E_0 , cutoff energy E_{cut} , and photon index Γ . To perform the maximum likelihood fit, we used the P8R2_SOURCE_V6 instrument response functions with the *Fermi* Science Tools version v11r05p02 and the NewMunit fitting function.²¹ The isotropic diffuse model was `iso_P8R2_SOURCE_V6_v06.txt`,²² with normalization left free, and the Galactic diffuse model (Acero et al. 2016) was `gll_iem_v06.fits`, with index and normalization left free. In the initial fit, we held all values at the 3FGL catalog values except for the spectral parameters for the target source, and the normalization for sources within 6° of the target or flagged in the 3FGL catalog as being variable. We inspected the residuals map and found that one additional source at $\alpha = 218.281^\circ$, $\delta = -17.992^\circ$ was required to model the region, so this was added to the model. This source is positionally associated with the quasi-stellar object PKS 1430–178. The best-fit spectral parameters for the pulsar are presented in Table 4, where the “Test Statistic” (TS) is the source detection significance (Mattox et al. 1996). The exponentially cutoff power law model is preferred to a pure power law with a confidence of $4\text{-}\sigma$ ($\text{TS}_{\text{cut}} = 2\Delta \log(\text{likelihood})$ between the model with and without the cutoff). We then used `gtfindsrc` to get an improved localization for the LAT source, which gave a position of $\alpha = 210.166^\circ$, $\delta = -14.535^\circ$ (only $0.7'$ from the radio timing position) with a 95% confidence radius of $3.3'$.

For the timing analysis, we selected photons from a region of radius 2° around the pulsar and assigned photon weights based on the best-fit spectral model. We computed a pulse phase for each selected LAT photon using the `fermi` plugin for TEMPO2 (Ray et al. 2011) and the best-fit radio timing model. The pulsation significance was determined using the weighted H-test (Kerr 2011) and the resulting H-test value was 17.4, corresponding

²¹ <https://fermi.gsfc.nasa.gov/ssc/data/analysis/documentation/>

²² <https://fermi.gsfc.nasa.gov/ssc/data/access/lat/BackgroundModels.html>

Table 3
Summary of Optical Observations of PSR J1400–1431

Telescope/Instrument	Date	Filter	Airmass	Exposure (sec)	Magnitude
SOAR/Goodman	2016-06-09	R_c	1.81	46×5	22.5 ± 0.3
Keck I/LRIS(blue)	2016-08-02	V	2.03	180	23.41 ± 0.08
Keck I/LRIS(red)	2016-08-02	R	1.71	300	22.52 ± 0.04
Keck I/LRIS(red)	2016-08-02	I	1.92	300	21.99 ± 0.04

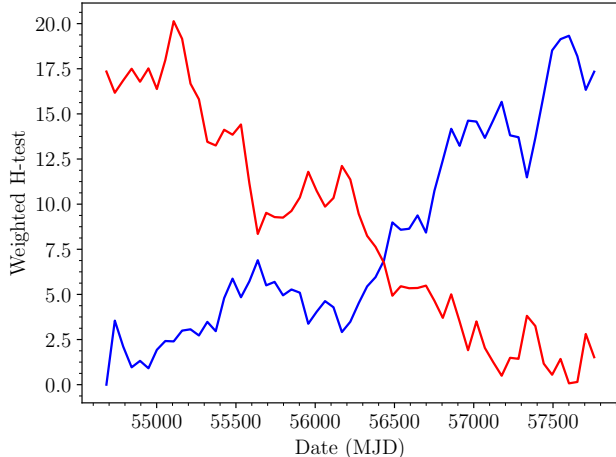


Figure 7. Weighted H-test vs time computed both forwards (blue) and backwards (red) in time. While the H-test does not reach the $5\text{-}\sigma$ level, the rising H-test is indicative of a marginally-detected pulsation. The mostly monotonic rise is an indication that the pulse timing model used to fold the data is phase-coherent over the full LAT mission.

to a significance of $3.3\text{-}\sigma$ (see Figure 7). This is not sufficient to claim a secure detection, but suggests that weak LAT pulsations may be present from this source.

Although there is only weak evidence for the presence of pulsations, we find strong support for an association between 3FGL J1400.5–1437 and PSR J1400–1431, primarily due to their positional coincidence. The GeV spectrum of the 3FGL source shows significant curvature, providing additional support for an association. Also, Γ and E_{cut} values are comparable to those of other MSPs in the Fermi Second Pulsar Catalog (2PC; Abdo et al. 2013). Finally, the marginal detection of pulsations provides additional evidence in favor of the identification of the γ -ray source with the pulsar, though not with certainty. Assuming this association is real, we can compare it to the rest of the MSP population, which are often γ -ray emitters.

Since the DC (constant/non-pulsed) γ -ray source is strongly detected (a TS of 391 corresponds to a detection significance of $17\text{-}\sigma$) we might expect to see detectable pulsations. Figure 8 shows the correlation between DC source TS and the weighted H-test for pulsations, based on data from 2PC. Clearly, the pulsed significance for J1400–1431 is far below what is expected based on its γ -ray flux. Assuming the pulse timing model is good, this indicates either a low pulsed fraction, or a sinusoidal (rather than sharply-peaked) pulse profile, or both, hampering the detection of pulsed emission.

5. X-RAY OBSERVATIONS

PSR J1400–1431 was targeted with the X-ray Multi-Mirror Mission, *XMM-Newton* on 2016 July 17 for a duration of 39.8 ks (ObsID 0780670101; PI S. Bogdanov). The European Photon Imaging Camera (EPIC) pn (Strüder et al. 2001) and MOS1/2 (Turner et al.

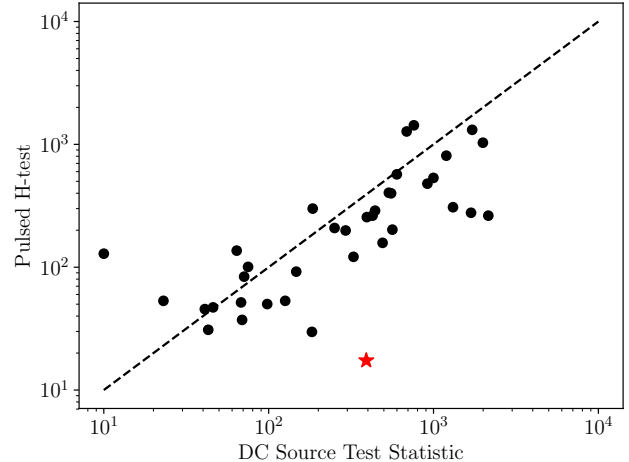


Figure 8. Weighted H-test statistic vs. Test Statistic for the DC γ -ray source for the sample of MSPs in 2PC (Abdo et al. 2013). The red star shows PSR J1400–1431.

Table 4
LAT Spectral Analysis Results

Parameter	Value
3FGL Source.....	J1400.5–1437
Γ	2.1(1)
E_{cut} (GeV).....	4.7(17)
Photon flux ^a ($\times 10^{-9}$ ph cm ⁻² s ⁻¹).....	20(2)
Energy flux ^a ($\times 10^{-12}$ erg cm ⁻² s ⁻¹).....	10.2(6)
TS.....	391
TS _{cut}	17.7

Note. — Quantities in parentheses are 68% confidence uncertainties (statistical only) in the last digit.

^a Over the 0.1 – 100 GeV energy range.

2001) instruments were configured in *full window mode* and used the thin optical blocking filters. We reprocessed the observation data files using the *XMM-Newton* Science Analysis Software (SAS²³) version `xmmsas_20160201_1833-15.0.0`. The data were subjected to the standard flag, pattern, and pulse invariant filtering. Periods of strong background flares were excised, which resulted in effective exposures of 35.4, 36.3, and 28.2 ks for the MOS1, MOS2, and pn, respectively. The cleaned data sets were used for the X-ray spectroscopic analysis presented below. Due to the 0.73 s read-out time of the pn and 2.6 s for MOS1/2, it was not possible to fold the data at the MSP period to study any X-ray pulsations.

Figure 9 shows the co-added representative color image from all three *XMM-Newton* detectors. It is evi-

²³ The *XMM-Newton* SAS is developed and maintained by the Science Operations Centre at the European Space Astronomy Centre and the Survey Science Centre at the University of Leicester.

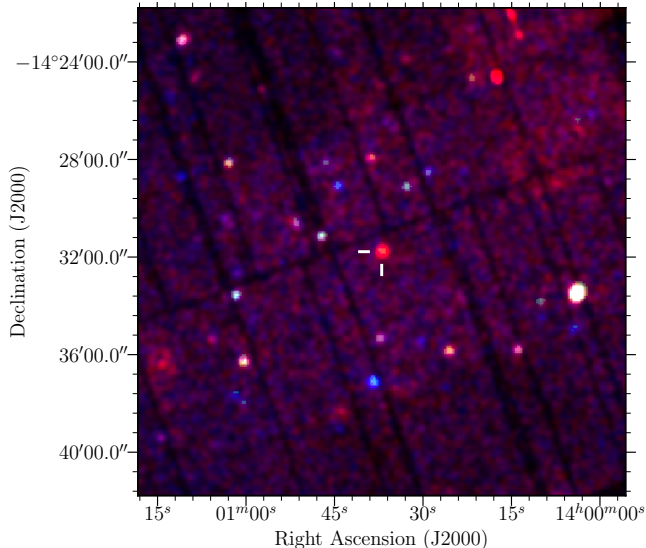


Figure 9. A “true color” image of the combined *XMM-Newton* EPIC MOS1, MOS2 and pn data of PSR J1400–1431 with red corresponding to 0.3 – 1 keV, green to 1 – 2 keV, and blue to 2 – 7 keV. The pulsar is a faint and soft X-ray source (typical of MSPs) and is marked by the two white ticks near the center of the image.

dent that PSR J1400–1431 is a faint X-ray source and it is quite soft, with nearly all source photons detected below ~ 1.5 keV. To produce spectra suitable for fitting, the pn, MOS1, and MOS2 data were grouped such that each energy bin contained at least 25 counts. The binned spectra from all three detectors were modeled jointly in XSPEC. Three single-component models were considered: a power law, a blackbody, and a non-magnetic neutron star hydrogen atmosphere model (NSATMOS; Heinke et al. 2006). Due to the limited photon statistics, in the spectroscopic analysis we fix the value of the equivalent atomic hydrogen column density, $N_{\text{H}} = 1.5 \times 10^{20} \text{ cm}^{-2}$, determined from the empirical relation between DM and N_{H} from He et al. (2013). In all cases, the `tbabs` model (Wilms et al. 2000) was used to account for the interstellar absorption along the line of sight.

A fit with a power law produces statistically acceptable results ($\chi^2_{\nu} = 1.02$ for 21 degrees of freedom) but requires an implausibly steep power law photon index ($\Gamma \approx 6.5$). A blackbody model yields a temperature of $kT = 0.15 \pm 0.02$ keV, an effective emitting radius of $R_{\text{eff}} = 0.06^{+0.05}_{-0.04}$ km, an unabsorbed flux of $(1.07 \pm 0.15) \times 10^{-14} \text{ erg cm}^{-2} \text{ s}^{-1}$ in the 0.3–10 keV range, and $\chi^2_{\nu} = 0.70$ for 21 degrees of freedom. Fitting a hydrogen atmosphere model assuming a neutron star with mass $1.4 M_{\odot}$, radius 12 km, and distance 270 pc resulted in a best-fit with a redshift-corrected effective temperature $T_{\text{eff}} = 7.8^{+1.5}_{-1.3} \times 10^5$ K, an emitting area that is $0.60^{+0.08}_{-0.04}\%$ of the total neutron star surface area, an unabsorbed 0.3–10 keV flux of $(1.15 \pm 0.17) \times 10^{-14} \text{ erg cm}^{-2} \text{ s}^{-1}$, and $\chi^2_{\nu} = 0.84$ for 21 degrees of freedom. The soft thermal spectrum of PSR J1400–1431 is typical of the sample of MSPs detected in X-rays (Zavlin 2006; Bogdanov et al. 2006; Forestell et al. 2014). This thermal radiation likely originates from the magnetic polar caps of the pulsar, which are heated to $\sim 10^6$ K by a return flow of relativistic particles from the open field region of the magnetosphere (e.g. Harding & Muslimov 2002).

6. DISCUSSION

With pulsar timing, we have measured J1400–1431’s parallax and find that \dot{P}_{meas} and μ_{T} values place an upper limit on the pulsar’s distance, which further constrains parallax and intrinsic spin-down. Combining these priors with another that accounts for the Lutz-Kelker bias, we find 95% confidence intervals on parallax ($\varpi = 3.7^{+1.6}_{-1.2}$ mas) and distance ($d = 270^{+130}_{-80}$ pc) respectively. Furthermore, astrometric parameter measurements imply $\dot{P}_{\text{Shklov}} = 7(2) \times 10^{-21}$, limiting intrinsic spin-down to $\dot{P}_{\text{int}} \lesssim 2.2 \times 10^{-21}$; only four other MSPs in the Galactic field (excluding those in globular clusters) have \dot{P}_{int} values this low (Manchester et al. 2005). For J1400–1431 this has interesting implications for other derived parameters such as characteristic age, $\tau > 22$ Gyr. The fact that $\tau > \tau_{\text{Hubble}}$ is not particularly concerning since it is well known that characteristic age derived in this fashion is a poor predictor of a recycled pulsar’s true age (e.g. Camilo et al. 1994b; Lorimer et al. 1995). Using WD cooling models (Tremblay et al. 2011; Bergeron et al. 2011), we find more realistic cooling timescales, $5 < \tau_{\text{cool}} < 9$ Gyr for assumed WD masses between 0.2 – 0.4 M_{\odot} . Since the WD is born as the recycling process concludes, τ_{cool} is a better indicator of the system’s true age. Assuming the true age of the pulsar is inside this range and magnetic dipole braking is entirely responsible for its spin-down (i.e. its braking index, $n = 3$), J1400–1431’s post-recycling birth period was likely between 2.4–2.7 ms, given a value of \dot{P}_{int} close to the limit shown in Table 2. This result is insensitive to the choice of n ; braking indices $1 < n < 3$ produce nearly identical ranges for birth period.

Since \dot{P}_{int} is proportional to the intrinsic spin-down luminosity (\dot{E}_{int}), J1400–1431’s low \dot{P}_{int} value likely also affects its high-energy emission. Typically X-ray and γ -ray luminosities, L_{X} and L_{γ} , are expressed as a fraction of \dot{E}_{int} with corresponding efficiencies, $\eta_{\text{X}} \equiv L_{\text{X}}/\dot{E}$ and $\eta_{\gamma} \equiv L_{\gamma}/\dot{E}$; values for these efficiencies have been found in the ranges $0.001\% < \eta_{\text{X}} < 0.1\%$ (see Figure 8 of Forestell et al. 2014) and $1\% < \eta_{\gamma} < 100\%$ (Guillemot et al. 2016). Contours within these ranges are highlighted in Figure 11. After correcting for the Shklovskii effect, J1400–1431’s spin-down luminosity is $\dot{E}_{\text{int}} < 3.0 \times 10^{33} \text{ erg s}^{-1}$ (see Table 2).

Using a nominal distance of 270 pc and assuming a beaming factor $f_{\Omega} = 1$, the γ -ray luminosity $L_{\gamma} = 4\pi f_{\Omega} d^2 F_{\gamma} = 8.9 \times 10^{31} \text{ erg s}^{-1}$ (see Eq. 15 from Abdo et al. 2013, and description therein), where F_{γ} is the measured γ -ray energy flux from Table 4. Based on the implied γ -ray efficiency of $\eta_{\gamma} \gtrsim 3\%$ – on the low-end of efficiencies found for MSPs in 2PC – the pulsar produces plenty of energy to power the γ -ray source. We also note that $\dot{E}_{\text{int}}/d^2 = 7.4 \times 10^{34} \text{ erg s}^{-1} \text{ kpc}^{-2}$, which is very high owing to the small distance. Over 75% of radio MSPs with $\dot{E}_{\text{int}}/d^2 > 1.5 \times 10^{34} \text{ erg s}^{-1} \text{ kpc}^{-2}$ have LAT-detected γ -ray pulsations (Guillemot & Tauris 2014). Evidently, as observed from Earth, J1400–1431 is relatively inefficient at converting spin-down luminosity into γ -ray emission, and given the flux of the γ -ray emission, the modulation is more difficult to detect than for most other MSPs.

The X-ray luminosity of $1 \times 10^{29} \text{ ergs s}^{-1}$ (0.3–10 keV; $d = 270$ pc) makes J1400–1431 the least X-ray luminous rotation-powered MSP detected to date. For reference, it is more than an order of magnitude fainter than other nearby MSPs – PSRs J0437–4715, J2124–3358

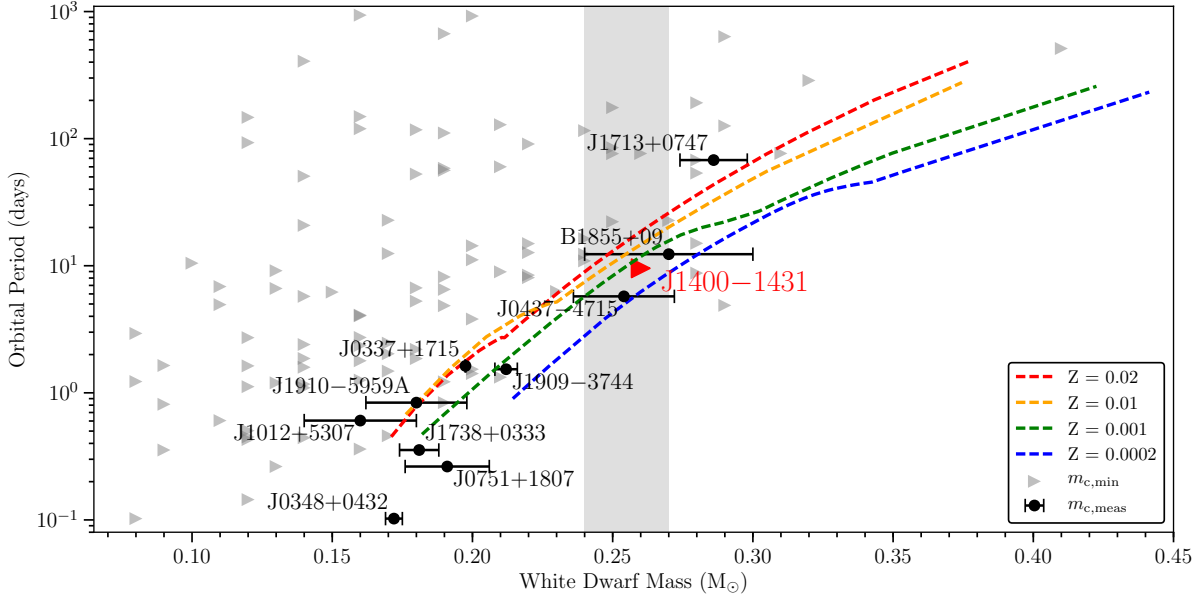


Figure 10. Colored dashed lines show the (P_b, m_{WD}) -relationship expected for He WD populations, simulated with corresponding metallicities listed in the legend (Istrate et al. 2016). Minimum companion masses (gray triangles) determined with pulsar timing and measured WD masses (black circles) from Manchester et al. (2005) are also plotted. The red triangle shows $m_{c,\text{min}} = 0.26 M_\odot$ derived with pulsar timing for J1400–1431’s WD companion and the gray shaded region indicates masses consistent with Istrate et al. (2016) models given $P_B = 9.5$ days, $0.24 < m_c < 0.27 M_\odot$.

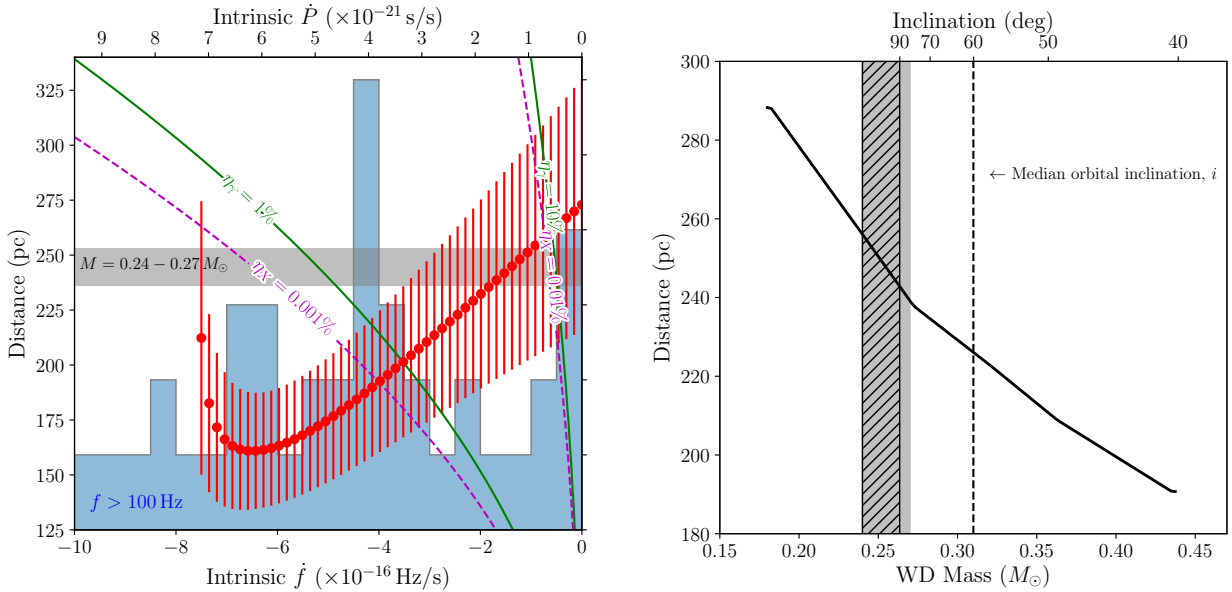


Figure 11. *Left:* Predicted distance as a function of intrinsic spin-down \dot{f} for PSR J1400–1431, based on Eqn. 5. The red points show the 68% confidence range for the distance posteriors. The grey band shows the inferred range of distance for companion masses of $0.24 - 0.27 M_\odot$, which is the range inferred from Fig. 10, based on the models of low-mass white dwarfs from Althaus et al. (2013) computed for $T_{\text{eff}} = 3000$ K and linearly interpolated for this mass range. We also show contours of the inferred X-ray and γ -ray efficiencies η_X and η_γ . Values of η_X between 0.001% and 0.01% are consistent with the inferred distance range and are reasonable given Forestell et al. (2014), just as values of η_γ between 1% and 10% are consistent with the data and are reasonable given Guillemot et al. (2016). Finally, the blue histogram shows the distribution of \dot{f} for millisecond pulsars ($f > 100$ Hz) that are not in globular clusters based on Manchester et al. (2005); they have been corrected for the Shklovskii effect as well as possible given the data in the catalog. Note that the top \dot{P} axis is only correct for a source with the spin period of PSR J1400–1431 (3.1 ms). *Right:* We show the same range of masses as indicated on the left-hand plot ($m_c = 0.24 - 0.27 M_\odot$) and explicitly plot how distance scales with WD mass based on Althaus et al. (2013) models and our photometry results noted in §3. The top axis shows inclination angles corresponding to various WD masses and the hatched region shows WD masses excluded by $m_{c,\text{min}}$; derived values assume $m_p = 1.35 M_\odot$.

(Zavlin 2006), and J0030+0451 (Bogdanov & Grindlay 2009) – all of which have luminosities of 10^{30} erg s $^{-1}$ or higher. This striking difference can be attributed to J1400–1431’s much smaller spin-down luminosity (\dot{E}); the implied conversion efficiency from spin-down to X-ray luminosity for J1400–1431 is $\eta_X > 3.3 \times 10^{-5}$, consistent with $10^{-5} < \eta_X < 10^{-3}$ typically found for MSPs. On the other hand, if \dot{E}_{int} is close to the derived upper limit, the low X-ray luminosity might be an indication that the polar cap heating mechanism operates less efficiently in J1400–1431 for reasons that remain to be understood.

PSR J1400–1431 is in a nearly circular, 9.5 day orbit around its WD companion, which has a minimum mass of $m_{c,\text{min}} = 0.26 M_\odot$ (assuming $m_p = 1.35 M_\odot$). Interestingly, this value is in remarkable agreement with the predicted (P_b, m_{WD}) -relationship (see Figure 10). The correlation between P_b and WD mass is an expected result of the relationship between the He-core mass and radius of a low-mass, red giant donor star, regardless of the mass present in its outer envelope (Savonije 1987; Tauris & Savonije 1999). Most WDs with measured masses follow this expected relationship (see Figure 10). The WD companion of PSR J1640+2224 is the most obvious exception, but was removed from Figure 10 due to inconsistent conclusions about its mass based on pulsar timing and astrometric follow-up (S. Vigeland, private communication). Otherwise, only two $m_{c,\text{min}}$ values are inconsistent with predicted curves.²⁴ Istrate et al. (2016) show that the (P_b, m_{WD}) -relationship has some width, depending on the metallicity of the progenitor of the WD companion. By allowing a range of m_p , i and WD progenitor metallicities for J1400–1431’s companion, we find a narrow range of $m_c = 0.24 - 0.27 M_\odot$ for $P_b = 9.5$ days (see Figure 10). The WD mass inferred from the (P_b, m_{WD}) -relationship is quite close to $m_{c,\text{min}}$ (for $m_p = 1.35 M_\odot$), suggesting the system is highly inclined. However, there is considerable uncertainty in the (P_b, m_{WD}) -relation not only as a function of metallicity (as plotted) but due to the unknown history of the system, so it is also worth considering alternate constraints on the inclination.

For millisecond pulsars in highly-inclined orbits, a Shapiro delay signature is sometimes detectable in its timing residuals as a function of orbital phase.²⁵ The maximum delay occurs at superior conjunction (orbital phase, $\phi_{\text{orb}} = 0.25$), when the pulsar’s signal must travel directly through its companion’s gravitational well along our line of sight. If J1400–1431 were as highly inclined as discussed above, we would expect a Shapiro delay, $\Delta_{\text{SB}} = 11 \mu\text{s}$ at superior conjunction (for $m_c = 0.27 M_\odot$ and $i = 80^\circ$), which we do not see (Figure 12). However, going to the median expected inclination of 60° results in a qualitatively similar companion mass, $0.31 M_\odot$, with a significant reduction in the Shapiro delay to $6 \mu\text{s}$, which would not be detectable with the current data. Note that a smaller pulsar mass could also reduce the significance of any Shapiro delay by moving to a lower implied inclination angle to match the (P_b, m_{WD}) -relation. We expect to be able to put better constraints on range and shape parameters after analyzing data from an upcoming, targeted Shapiro delay observing campaign.

²⁴ These points correspond to PSRs J1125–6014 (Lorimer et al. 2006) and J1748–2446W (Ransom et al. 2005), but there is no mention in the literature of them being inconsistent with the expected (P_b, m_{WD}) -relationship.

²⁵ We use *orbital phase* interchangeably with *eccentric anomaly*, since J1400–1431’s orbit is nearly circular.

We can further constrain the WD companion’s mass using models (e.g. Althaus et al. 2013) that provide mass–radius relationships for low-mass WDs, photometry results from §3 and the posterior PDF for distance (see Figure 3), derived from pulsar timing. Figure 11 (right panel) shows the conversion between WD mass and distance, which could further be expressed as a prior in m_c -space; taking into account the low-significance parallax detection and additional priors mentioned in §2.2, a similar conversion effectively sets an upper limit on $m_c \lesssim 0.4 M_\odot$.

Figure 11 (left panel) shows the remarkable agreement between the mass range predicted by the (P_b, m_{WD}) -relationship, our distance posterior (taking into account a significant \dot{P}_{Shklov}), photometry results, and estimated X-ray and γ -ray efficiencies. The significant proper motion measured for J1400–1431 suggests that $\dot{P}_{\text{int}} < 2.2 \times 10^{-21}$, which is low, but still consistent with known values for other MSPs in the Galactic field whose intrinsic \dot{P} values have been corrected for the Shklovskii effect. Figure 11 (right panel) shows how the $m_c = 0.24 - 0.27 M_\odot$ range is mostly excluded, simply based on $m_{c,\text{min}}$ (assuming $m_p = 1.35 M_\odot$), derived from timing results. The lack of detectable Shapiro delay implies a slightly higher companion mass and lower inclination angle. Despite slight inconsistency with the mass range implied by the (P_b, m_{WD}) -relationship, our data suggest J1400–1431’s companion mass is likely $\sim 0.30 M_\odot$ and the system is ≈ 230 pc away with an orbital inclination angle, $i \gtrsim 60^\circ$.

7. CONCLUSIONS

In this paper, we described follow-up timing efforts on PSR J1400–1431 since its discovery by high school students involved in the Pulsar Search Collaboratory was first reported in Rosen et al. (2013). Our updated solution includes TOAs spanning five years from timing observations conducted with the GBT at \sim monthly cadence. With the latest timing solution, we measure J1400–1431’s position to milli-arcsecond precision, its spin-down, proper motion, a monotonic slope in DM over time, and a weak parallax signature. Because of the pulsar’s significant total proper motion, a kinematic (Shklovskii) component accounts for a significant fraction of \dot{P}_{meas} and we can only place an upper limit on the intrinsic spin-down, $\dot{P}_{\text{int}} < 2.2 \times 10^{-21}$ s/s.

The Shklovskii effect provides an additional prior for the system’s parallax and in turn, better constraints on distance, $d = 270_{-80}^{+130}$ pc. This range agrees nicely with distances estimated using electron density models (270 – 500 pc; Taylor & Cordes 1993; Cordes & Lazio 2002; Yao et al. 2017).

Using the Goodman Spectrograph on the 4.1-m SOAR Telescope and later, the LRIS on the 10-m Keck I Telescope for deeper imaging, we detected J1400–1431’s WD companion for the first time. Photometry suggests the companion is a cool, DA-type WD (Hydrogen atmosphere) with $T_{\text{eff}} = 3000 \pm 100$ K and $R/R_\odot = (2.19 \pm 0.03) \times 10^{-2}$ ($d/270$ pc). Combined with WD cooling models, the effective temperature measurement suggests that the system’s age is in the range 5–9 Gyr, which is consistent with the relatively low upper limit we place on \dot{P}_{int} after correcting for the Shklovskii effect and the corresponding characteristic age. Using WD mass-radius models from Althaus et al. (2013) and photometric R/d , we find implied mass and distance ranges completely consistent with $m_{c,\text{min}} = 0.26 M_\odot$ and $d = 270_{-80}^{+130}$ pc mea-

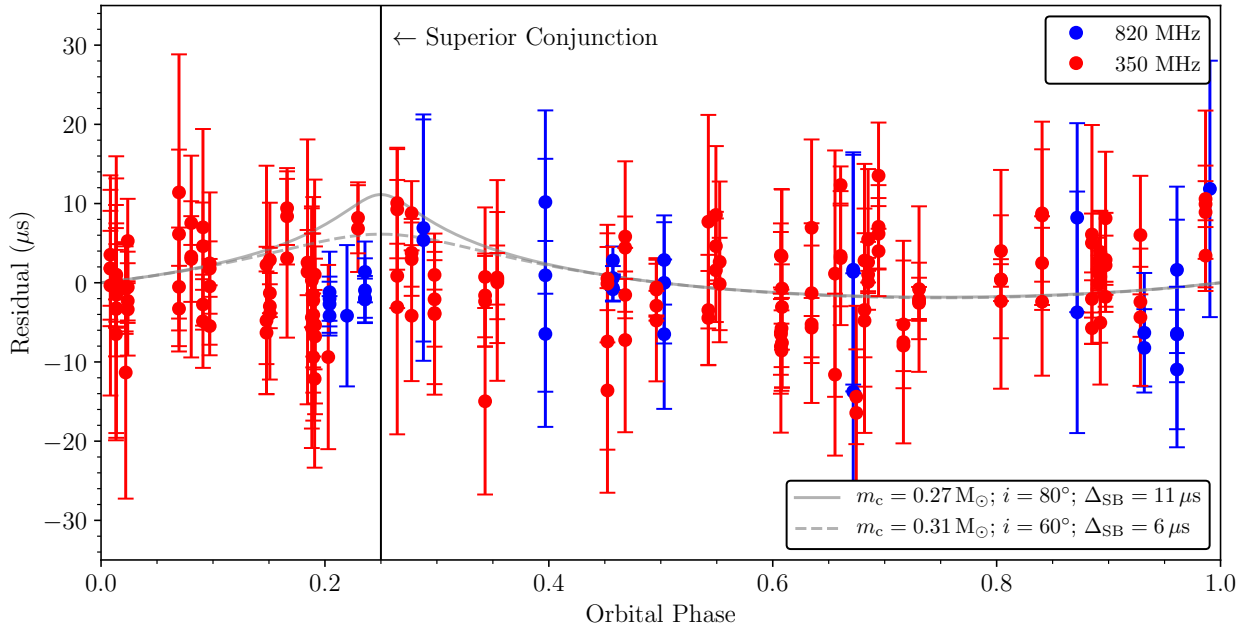


Figure 12. Timing residuals in microseconds for J1400–1431, plotted as a function of orbital phase. Observations at 350 MHz and 820 MHz are shown in red and blue, respectively. The solid/dashed gray lines show expected Shapiro delays, given assumed combinations of companion mass (m_c) and orbital inclination angle (i). With these assumptions, the expected delays at superior conjunction ($\phi_{\text{orb}} = 0.25$) are $11 \mu\text{s}$ (solid) and $6 \mu\text{s}$ (dashed) respectively.

surements.

Finally, with high-energy detections of J1400–1431 with *XMM-Newton* and *Fermi*, we measured X-ray and γ -ray luminosities, $L_X = 1 \times 10^{29} \text{ ergs s}^{-1}$ and $L_\gamma = 8.9 \times 10^{31} \text{ ergs s}^{-1}$, respectively. Given the upper limit on \dot{P}_{int} (and therefore \dot{E}_{int}), we find efficiencies $\eta_X > 3.3 \times 10^{-5}$ and $\eta_\gamma \gtrsim 0.03$, consistent with expected ranges for respective wavelength regimes. Although measured high-energy luminosities depend on the assumed nominal distance ($d = 270 \text{ pc}$), corresponding efficiencies provide additional consistency checks on \dot{P}_{int} , distance and photometry constraints determined with various methods.

This information presents a consistent picture; combined, it suggests PSR J1400–1431 has an intrinsic spindown $\dot{P}_{\text{int}} \approx 2 \times 10^{-21} \text{ s/s}$, a distance $d \approx 230 \text{ pc}$, WD companion mass $m_c \sim 0.30 M_\odot$, and orbital inclination $i \gtrsim 60^\circ$. These conclusions are slightly inconsistent with WD evolution models (e.g. Istrate et al. 2016) and depend on an assumed pulsar mass ($m_p = 1.35 M_\odot$), but our results are relatively insensitive to m_p . Even for low orbital inclination angles ($i \sim 60^\circ$), we expect a Shapiro delay signature to be detectable ($\Delta_{\text{SB}} = 6 \mu\text{s}$) with data from an upcoming, targeted observing campaign, which will provide further clarity on results presented here.

ACKNOWLEDGMENTS

The Green Bank Observatory is a facility of the National Science Foundation operated under cooperative agreement by Associated Universities, Inc.

JKS, DLK, MAM, DRL, PSR, RL, PG, and KS are supported by the NANOGrav NSF Physics Frontiers Center award number 1430284. Portions of this research performed at the Naval Research Laboratory are supported by NASA. RH, AV, PC, and BB would like to thank the High Point University (HPU) Student Government Association for providing travel funds to Cerro Tololo/Pachon; the HPU Summer Undergraduate Research Program in the Sciences for providing summer research support; and President Qubein, Provost Car-

roll, and Dean Stoneking for their generous support of the sciences at HPU. AGI acknowledges support from the NASA Astrophysics Theory Program through NASA grant NNX13AH43G.

We thank Matthew Kerr for providing the 2PC H-test values. The *Fermi* LAT Collaboration acknowledges generous ongoing support from a number of agencies and institutes that have supported both the development and the operation of the LAT as well as scientific data analysis. These include the National Aeronautics and Space Administration and the Department of Energy in the United States, the Commissariat à l’Energie Atomique and the Centre National de la Recherche Scientifique / Institut National de Physique Nucléaire et de Physique des Particules in France, the Agenzia Spaziale Italiana and the Istituto Nazionale di Fisica Nucleare in Italy, the Ministry of Education, Culture, Sports, Science and Technology (MEXT), High Energy Accelerator Research Organization (KEK) and Japan Aerospace Exploration Agency (JAXA) in Japan, and the K. A. Wallenberg Foundation, the Swedish Research Council and the Swedish National Space Board in Sweden. Additional support for science analysis during the operations phase is gratefully acknowledged from the Istituto Nazionale di Astrofisica in Italy and the Centre National d’Études Spatiales in France.

A portion of the results presented was based on observations obtained with *XMM-Newton*, an ESA science mission with instruments and contributions directly funded by ESA member states and NASA.

This paper is based (in part) on data obtained with the International LOFAR Telescope (ILT). LOFAR (van Haarlem et al. 2013) is the Low Frequency Array designed and constructed by ASTRON. It has facilities in several countries, that are owned by various parties (each with their own funding sources), and that are collectively operated by the ILT foundation under a joint scientific policy.

Facilities: GBT (GUPPI), *Fermi* LAT, *XMM-Newton*

(pn, MOS1/2), Keck I: 10-m (LRIS), SOAR: 4.1-m (Goodman Spectrograph), LOFAR, LWA

Software: libstempo, astropy (Astropy Collaboration et al. 2013), scipy (Jones et al. 2001), TEMPO, TEMPO2 (Hobbs et al. 2006), PSRCHIVE (Hotan et al. 2004c), IRAF/DAOPHOT, LPIPE, SExtractor (Bertin & Arnouts 1996), *Fermi* Science Tools

REFERENCES

- Abdo, A. A., Ajello, M., Allafort, A., et al. 2013, *ApJS*, 208, 17
- Acero, F., Ackermann, M., Ajello, M., et al. 2015, *ApJS*, 218, 23 — 2016, *ApJS*, 223, 26
- Althaus, L. G., Miller Bertolami, M. M., & Córscico, A. H. 2013, *A&A*, 557, A19
- Arzoumanian, Z., Brazier, A., Burke-Spolaor, S., et al. 2015, *ArXiv e-prints*, arXiv:1505.07540
- Astropy Collaboration, Robitaille, T. P., Tollerud, E. J., et al. 2013, *A&A*, 558, A33
- Backer, D. C., & Hellings, R. W. 1986, *ARA&A*, 24, 537
- Becker, W. 2009, in *Astrophysics and Space Science Library*, Vol. 357, Astrophysics and Space Science Library, ed. W. Becker, 91
- Bergeron, P., Saumon, D., & Wesemael, F. 1995, *ApJ*, 443, 764
- Bergeron, P., Wesemael, F., Dufour, P., et al. 2011, *ApJ*, 737, 28
- Bertin, E., & Arnouts, S. 1996, *A&AS*, 117, 393
- Bessell, M. S. 1986, *PASP*, 98, 1303
- Bogdanov, S., & Grindlay, J. E. 2009, *ApJ*, 703, 1557
- Bogdanov, S., Grindlay, J. E., Heinke, C. O., et al. 2006, *ApJ*, 646, 1104
- Boyles, J., Lynch, R. S., Ransom, S. M., et al. 2013, *ApJ*, 763, 80
- Briskin, W. F., Benson, J. M., Goss, W. M., & Thorsett, S. E. 2002, *ApJ*, 571, 906
- Camilo, F., Foster, R. S., & Wolszczan, A. 1994a, *ApJL*, 437, L39
- Camilo, F., Thorsett, S. E., & Kulkarni, S. R. 1994b, *ApJL*, 421, L15
- Chambers, K. C., Magnier, E. A., Metcalfe, N., et al. 2016, *ArXiv e-prints*, arXiv:1612.05560
- Chatterjee, S., Briskin, W. F., Vlemmings, W. H. T., et al. 2009, *ApJ*, 698, 250
- Clemens, J. C., Crain, J. A., & Anderson, R. 2004, in *Proc. SPIE*, Vol. 5492, Ground-based Instrumentation for Astronomy, ed. A. F. M. Moorwood & M. Iye, 331–340
- Cordes, J. M., & Lazio, T. J. W. 2002, *ArXiv Astrophysics e-prints*, astro-ph/0207156
- Demorest, P. B., Ferdman, R. D., Gonzalez, M. E., et al. 2013, *ApJ*, 762, 94
- Desvignes, G., Caballero, R. N., Lentati, L., et al. 2016, *MNRAS*, 458, 3341
- DuPlain, R., Ransom, S., Demorest, P., et al. 2008, in *Society of Photo-Optical Instrumentation Engineers (SPIE) Conference Series*, Vol. 7019, Society of Photo-Optical Instrumentation Engineers (SPIE) Conference Series, 1
- Efron, B. 1979, *Ann. Statist.*, 7, 1
<http://dx.doi.org/10.1214/aos/1176344552>
- Flewelling, H. A., Magnier, E. A., Chambers, K. C., et al. 2016, *ArXiv e-prints*, arXiv:1612.05243
- Forestell, L. M., Heinke, C. O., Cohn, H. N., et al. 2014, *MNRAS*, 441, 757
- Guillemot, L., & Tauris, T. M. 2014, *MNRAS*, 439, 2033
- Guillemot, L., Smith, D. A., Laffon, H., et al. 2016, *A&A*, 587, A109
- Hansen, B. M. S. 1998, *Nature*, 394, 860
- Harding, A. K., & Muslimov, A. G. 2002, *ApJ*, 568, 862
- He, C., Ng, C.-Y., & Kaspi, V. M. 2013, *ApJ*, 768, 64
- Heinke, C. O., Rybicki, G. B., Narayan, R., & Grindlay, J. E. 2006, *ApJ*, 644, 1090
- Hobbs, G., Lorimer, D. R., Lyne, A. G., & Kramer, M. 2005, *MNRAS*, 360, 974
- Hobbs, G. B., Edwards, R. T., & Manchester, R. N. 2006, *MNRAS*, 369, 655
- Hotan, A. W., Bailes, M., & Ord, S. M. 2004a, *MNRAS*, 355, 941
- Hotan, A. W., van Straten, W., & Manchester, R. N. 2004b, *PASA*, 21, 302
- 2004c, *PASA*, 21, 302
- Istrate, A. G., Marchant, P., Tauris, T. M., et al. 2016, *A&A*, 595, A35
- Jacoby, B. A., Bailes, M., van Kerkwijk, M. H., et al. 2003, *ApJL*, 599, L99
- Jones, E., Oliphant, T., Peterson, P., et al. 2001, *SciPy: Open source scientific tools for Python*, , [Online; accessed 2017-03-06]. <http://www.scipy.org/>
- Kaspi, V. M., Taylor, J. H., & Ryba, M. F. 1994, *ApJ*, 428, 713
- Kerr, M. 2011, *ApJ*, 732, 38
- Kondratiev, V. I., Verbiest, J. P. W., Hessels, J. W. T., et al. 2016, *A&A*, 585, A128
- Lang, D., Hogg, D. W., Mierle, K., Blanton, M., & Roweis, S. 2010, *AJ*, 139, 1782
- Lange, C., Camilo, F., Wex, N., et al. 2001, *MNRAS*, 326, 274
- Löhmer, O., Kramer, M., Driebe, T., et al. 2004, *A&A*, 426, 631
- Lommen, A. N., Kipporn, R. A., Nice, D. J., et al. 2006, *ApJ*, 642, 1012
- Lorimer, D. R., & Kramer, M. 2004, *Handbook of Pulsar Astronomy* (UK: Cambridge University Press)
- Lorimer, D. R., Lyne, A. G., Festin, L., & Nicastro, L. 1995, *Nature*, 376, 393
- Lorimer, D. R., Faulkner, A. J., Lyne, A. G., et al. 2006, *MNRAS*, 372, 777
- Lutz, T. E., & Kelker, D. H. 1973, *PASP*, 85, 573
- Lynch, R. S., Boyles, J., Ransom, S. M., et al. 2013, *ApJ*, 763, 81
- Manchester, R. N., Hobbs, G. B., Teoh, A., & Hobbs, M. 2005, *AJ*, 129, 1993
- Matthews, A. M., Nice, D. J., Fonseca, E., et al. 2016, *ApJ*, 818, 92
- Matttox, J. R., Bertsch, D. L., Chiang, J., et al. 1996, *ApJ*, 461, 396
- Monet, D. G., Levine, S. E., Canzian, B., et al. 2003, *AJ*, 125, 984
- Murphy, T., Kaplan, D. L., Bell, M. E., et al. 2017, *PASA*, 34, e020
- Nice, D. J., & Taylor, J. H. 1995, *ApJ*, 441, 429
- Oke, J. B., Cohen, J. G., Carr, M., et al. 1995, *PASP*, 107, 375
- Phinney, E. S., & Kulkarni, S. R. 1994, *ARA&A*, 32, 591
- Prinz, T., & Becker, W. 2015, *ArXiv e-prints*, arXiv:1511.07713
- Qi, Z., Yu, Y., Bucciarelli, B., et al. 2015, *AJ*, 150, 137
- Ransom, S. M., Hessels, J. W. T., Stairs, I. H., et al. 2005, *Science*, 307, 892
- Ray, P. S., Kerr, M., Parent, D., et al. 2011, *ApJS*, 194, 17
- Reardon, D. J., Hobbs, G., Coles, W., et al. 2016, *MNRAS*, 455, 1751
- Rosen, R., Swiggum, J., McLaughlin, M. A., et al. 2013, *ApJ*, 768, 85
- Sandhu, J. S., Bailes, M., Manchester, R. N., et al. 1997, *ApJL*, 478, L95
- Savonije, G. J. 1987, *Nature*, 325, 416
- Shklovskii, I. S. 1970, *Soviet Ast.*, 13, 562
- Splaver, E. M., Nice, D. J., Stairs, I. H., Lommen, A. N., & Backer, D. C. 2005, *ApJ*, 620, 405
- Stovall, K., Lynch, R. S., Ransom, S. M., et al. 2014, *ApJ*, 791, 67
- Stovall, K., Ray, P. S., Blythe, J., et al. 2015, *ApJ*, 808, 156
- Strüder, L., Briel, U., Dennerl, K., et al. 2001, *A&A*, 365, L18
- Tauris, T. M., & Savonije, G. J. 1999, *A&A*, 350, 928
- Taylor, G. B., Ellingson, S. W., Kassim, N. E., et al. 2012, *Journal of Astronomical Instrumentation*, 1, 1250004
- Taylor, J. H., & Cordes, J. M. 1993, *ApJ*, 411, 674
- Tody, D. 1986, in *Society of Photo-Optical Instrumentation Engineers (SPIE) Conference Series*, Vol. 627, Instrumentation in astronomy VI, ed. D. L. Crawford, 733
- Tonry, J. L., Stubbs, C. W., Lykke, K. R., et al. 2012, *ApJ*, 750, 99
- Toscano, M., Britton, M. C., Manchester, R. N., et al. 1999a, *ApJL*, 523, L171
- Toscano, M., Sandhu, J. S., Bailes, M., et al. 1999b, *MNRAS*, 307, 925
- Tremblay, P.-E., Bergeron, P., & Gianninas, A. 2011, *ApJ*, 730, 128
- Turner, M. J. L., Abbey, A., Arnaud, M., et al. 2001, *A&A*, 365, L27
- van Haarlem, M. P., Wise, M. W., Gunst, A. W., et al. 2013, *A&A*, 556, A2
- Verbiest, J. P. W., Lorimer, D. R., & McLaughlin, M. A. 2010, *MNRAS*, 405, 564
- Wilms, J., Allen, A., & McCray, R. 2000, *ApJ*, 542, 914
- Wolszczan, A., Doroshenko, O., Konacki, M., et al. 2000, *ApJ*, 528, 907
- Yao, J. M., Manchester, R. N., & Wang, N. 2017, *ApJ*, 835, 29
- Zavlin, V. E. 2006, *ApJ*, 638, 951